Advances in Geo-Energy Research

Original article

A multi-field coupling model for CO₂ enhanced shale gas recovery integrating chemical dissolution and mechanical weakening effects

Kang Yang¹, Yaobai Sun¹, Junping Zhou²⁰*, Qiao Chen¹, Guangrong Deng³, Dasong Li⁴

Keywords:

Shale reservoir CO₂ enhanced shale gas recovery chemical dissolution mechanical weakening permeability

Cited as:

Yang, K., Sun, Y., Zhou, J., Chen, Q., Deng, G., Li, D. A multi-field coupling model for CO₂ enhanced shale gas recovery integrating chemical dissolution and mechanical weakening effects. Advances in Geo-Energy Research, 2025, 18(2): 180-194. https://doi.org/10.46690/ager.2025.11.07

Abstract:

CO₂ enhanced shale gas recovery technology can effectively promote gas production and achieve CO₂ storage. The coupling relationship among the thermo-hydro-mechanical fields within the reservoir exhibits dynamic evolution during CO2 injection. Additionally, the geochemical interactions between shale and CO2 cause mineral dissolution and mechanical weakening, significantly influencing the shale reservoir characteristics. However, the impact mechanism of this coupling effect on CO₂ enhanced shale gas recovery is still unclear. This study first establishes and validates a thermo-hydro-mechanical-chemical coupling model. Then, the impacts of CO₂ injection on the reservoir physical characteristics and gas recovery under different influencing factors are investigated. The findings indicate that the relative permeability of the matrix and fractures in shale demonstrates an initial rapid increase, followed by a gradual decline during CO2 injection. This complex behavior is governed by the comprehensive impacts of effective stress evolution, competitive adsorption, chemical dissolution, and mechanical weakening. During the initial injection period, gas production and CO₂ storage increase rapidly as CO₂ injection pressure increases and injection temperature decreases, primarily governed by the effective stress and dissolution effect. During the middle and late injection periods, competitive adsorption-induced swelling and mechanical weakening effects are dominant, rendering the process highly sensitive to reservoir stress. At this stage, excessive injection pressure and excessively low temperatures accelerate permeability reduction. Consequently, when evaluating the efficacy of CO₂ enhanced shale gas recovery, it is essential to incorporate the coupling relationship between the chemical dissolution-mechanical weakening effect and thermohydro-mechanical fields of shale reservoir.

1. Introduction

The development of shale gas as a significant global natural gas resource is of great importance for the optimization of the energy structure. Recently, CO₂ enhanced shale gas recovery (CO₂-ESGR) technology has garnered significant attention

(Mansi et al., 2024; Yi et al., 2024). In this technology, supercritical CO₂ (ScCO₂) is injected into the reservoir to achieve shale reservoir fracturing. The high diffusivity and strong adsorption capacity of ScCO₂ are beneficial in replacing CH₄, greatly improving gas recovery (Bekeshov et al., 2023;

Yandy Scientific Press *Corresponding author.

E-mail address: yangkang@cigit.ac.cn (K. Yang); sunyaobai23@mails.ucas.ac.cn (Y. Sun); zhoujp1982@cqu.edu.cn (J. Zhou); chenqiao@cigit.ac.cn (Q. Chen); guangrong.deng@connect.polyu.hk (G. Deng); lidasongzz@163.com (D. Li). 2207-9963 © The Author(s) 2025.

¹Chongqing Institute of Green and Intelligent Technology, Chinese Academy of Sciences, Chongqing 400714, P. R. China

²State Key Laboratory of Coal Mine Disaster Dynamics and Control, Chongqing University, Chongqing 400044, P. R. China

³Department of Mechanical Engineering, Hong Kong Polytechnic University, Hong Kong 999077, P. R. China

⁴Chongqing River Affairs Center, Chongqing 401147, P. R. China

Meng et al., 2024; Zhao et al., 2024). Additionally, CO₂ storage in the reservoir can achieve greenhouse gas emission reduction (Wang et al., 2024a, 2024b). The process of CO₂ injection induces coupled alterations in the thermo-hydromechanical-chemical (THMC) fields within the shale reservoir (Zhao et al., 2020a; Zhou et al., 2022), accompanied by physicochemical reaction (e.g., matrix adsorption swelling, mineral dissolution) and mechanical weakening effects (e.g., strength and elastic modulus reduction) (Fatah et al., 2022a; Khosravi et al., 2023; Li et al., 2023b), which can affect gas production and reservoir stability. As a result, for the optimization of engineering parameters, it carries significant theoretical and engineering implications to establish a multiphysical field coupling model incorporating the mechanical weakening effect.

The continuous injection of CO₂ disrupts the geomechanical equilibrium of the reservoir during the CO₂-ESGR process. This gradual pressure increase reduces effective stress on the reservoir, thereby enlarging the pore apertures and consequently enhancing the permeability of shale (Song et al., 2024; Yang et al., 2022). Additionally, CH₄ in the reservoir is partially mixed with the injected CO₂ (Liu et al., 2015; Sun et al., 2025), which involves the competitive adsorption behavior of binary gas on shale. CH₄ desorption in shale induces shrinkage, while CO₂ adsorption causes swelling, which result in differential swelling, ultimately reducing both shale pore width and permeability (Klewiah et al., 2020; Wang et al., 2025). Due to the injection temperature of CO₂ being different from that of shale reservoir, heat convection and conduction also exist in the reservoir (Kim et al., 2017; Liu et al., 2021). This process involves thermal deformation, and alterations in the gas properties and adsorption characteristics, and ultimately affects shale permeability (Li et al., 2023a). To investigate the dynamic evolution of shale reservoir parameters under multiphysics coupling conditions, several theoretical models have been developed (Chen et al., 2025; Tang et al., 2023; Wan et al., 2024). These models typically conceptualize the shale as a dual-porosity system, with the gas within these structures existing predominantly in free and adsorbed states (Li and Elsworth, 2019; Mohagheghian et al., 2019; Zhang and Mehrabian, 2022). Based on this assumption, a coupling model incorporating multiple flow mechanisms during the CO₂-ESGR process was established (Kuang et al., 2024; Wang et al., 2025). Zhao et al. (2020a) incorporated temperature effects and developed a thermo-hydro-mechanical coupling model, which revealed that the relative position of injection wells and production wells both significantly affect the efficiency of CO₂-ESGR. Besides, the distribution of fractures significantly impacts fluid transport within the reservoir. Zhao et al. (2023) utilized a discrete fracture equation to analyze fluid transport within shale and investigated the impact of CO₂ injection parameters and reservoir parameters on shale gas production. While prior studies have predominantly focused on the coupling relationship between multi-physics fields within the reservoir during the CO₂-ESGR process and discussed the impacts of various injection parameters on this basis, they did not consider the influences of CO₂-shale interactions on the shale reservoir characteristics.

The injection of CO₂ into shale formations facilitates its transition to a supercritical state, given the reservoir conditions (pressure > 7.38 MPa, temperatures > 304.25 K) (Fatah et al., 2022b). This ScCO₂ interacts with shale during migration, triggering a series of geochemical reactions. These in turn dissolve the inorganic minerals within shale, thereby altering its pore structure (Memon et al., 2022; Ozotta et al., 2022; Oin et al., 2022a; Yang et al., 2024). Oin et al. (2022b) observed a decrease in the carbonate content of shale, and that the porosity after ScCO₂ exposure increased, which was triggered by the coupling impacts of extraction and dissolution effects. The mechanical properties of shale are also influenced by these chemical processes. Relevant studies have shown that ScCO₂ can weaken the mechanical characteristics of shale, decreasing its strength and elastic modulus (Choi et al., 2021; Zhou et al., 2021; Tan et al., 2022). Mineral dissolution and mechanical weakening effects caused by geochemical reactions synergistically influence shale permeability evolution (Cai et al., 2024). After ScCO₂ exposure, the permeability of shale increases under the influence of chemical effect (Deng et al., 2017; Zou et al., 2018). However, if the mechanical weakening effect is considered, it can be found that stress further compresses the pores increased by mineral dissolution, and the permeability decreases instead (Yang et al., 2022; Tian et al., 2023a, 2023b). The chemical dissolution and mechanical weakening effects of ScCO₂ on shale are also influenced by pressure and temperature. Prior studies have found that the dissolution degree of inorganic minerals in shale increases as CO₂ pressure rises and temperature declines, leading to both the expansion of pores and the weakening of mechanical properties (Yang et al., 2022, 2023, 2024). The above research results demonstrate that the permeability of shale is significantly influenced by the effects of chemical dissolution and mechanical weakening, and this process is also affected by the coupling impacts of reservoir stress, pressure and temperature. Current numerical simulations of CO₂-ESGR predominantly focus on hydro-mechanical or thermo-hydromechanical coupling. Although numerous THMC coupling models have been developed in other research fields, they primarily emphasize mineral dissolution effects, with limited consideration of the mechanical weakening induced by dissolution processes (Zhang et al., 2023). Besides, there is a lack of coupling models specifically tailored for CO₂-ESGR scenarios that integrate the physical and chemical interaction mechanisms between CO₂ and shale, the impact mechanism of this coupling effect on CO₂-ESGR is still unclear.

This study establishes and verifies a fully coupled THMC model incorporating the mechanical weakening effect, which comprehensively incorporates the impacts of effective stress, competitive adsorption, thermal expansion, chemical dissolution, and mechanical weakening on the permeability of shale. Furthermore, the impacts of CO₂ injection on shale gas production and reservoir physical characteristics under different influencing factors (reservoir stress, injection pressure, injection temperature, chemical dissolution-mechanical weakening effect) are analyzed. The findings provide valuable insights for optimizing CO₂-ESGR strategies.

2. Governing equations

The CO₂-ESGR process involves complex THMC coupling interactions. The continuous injection of CO₂ leads to partial mixing with CH₄, disrupting the stable state between stress and pressure in the shale reservoir. Additionally, CO₂ that is not in thermal equilibrium engages in heat transfer with the reservoir and the shale gas, altering the reservoir temperature distribution (Zhao et al., 2020a). Concurrently, the interaction of injected ScCO₂ with the shale triggers physical and chemical effects (such as differential adsorption-induced swelling of shale, chemical dissolution effect, etc.), significantly altering the pore structure and mechanical characteristics of shale (Zhou et al., 2021; Tan et al., 2022). These coupled THMC alterations collectively influence the CH₄/CO₂ fluid characteristics and shale deformation behaviors, thereby regulating gas transport capacity and ultimately affecting the efficiency of CO₂-ESGR (Fig. S1 in Supplementary file).

The CO₂-ESGR model established in this work mainly includes the deformation and stress of the reservoir, multicomponent gas diffusion and seepage, heat conduction, chemical dissolution, and mechanical weakening control equations. Given that the primary focus of this study is to analyze the response laws of shale reservoirs under THMC coupling, one of the important steps is to study the impact of coupled chemical dissolution-mechanical weakening effects on the reservoir parameters. Therefore, the model incorporates the following simplifying assumptions (Zhao et al., 2020b; Wang et al., 2025): (1) The stress-strain relationship of the shale reservoir is consistent with the generalized Hooke's law, as it is an isotropic linear elastic body. (2) Shale has a dualporosity structure, where the primary mechanism of gas flow within the matrix is diffusion, and the flow in the fractures is governed by Darcy's law. (3) The two primary forms of gas that exist in shale are free and adsorbed. (4) CH₄ adsorption in shale reaches a state of equilibrium before CO₂ injection, following the Langmuir isotherm for adsorption. Initially, the shale reservoir only contains CH₄. The gas-rich shale reservoir generally exhibits ultra-low water saturation, which is mainly bound water (Wang, 2010; Fang et al., 2014); therefore, the migration of gas-water two-phase flow within the shale reservoir is not considered.

2.1 Chemical dissolution-mechanical weakening equation

2.1.1 Porosity change in shale caused by chemical dissolution

The chemical dissolution of CO_2 -shale interaction on inorganic minerals increases the pore space and decreases the matrix width. The chemical dissolution damage (D_c) is defined to characterize the dissolution degree (Kachanov, 1999):

$$D_c = \frac{\Delta\phi_c}{1 - \phi_0} \times 100\% \tag{1}$$

where ϕ_0 denotes the initial porosity of shale before chemical dissolution; $\Delta\phi_c$ denotes the change of shale porosity before and after chemical dissolution, which can be expressed as (Tang et al., 2023):

$$\Delta \phi_c = -\frac{\Delta V_c}{V} = -\varepsilon_c \tag{2}$$

where ΔV_c denotes the shale volume change caused by chemical dissolution; V denotes the shale volume; ε_c denotes the volumetric strain caused by the chemical dissolution.

After combining Eqs. (1) and (2), ε_c and D_c can be expressed as:

$$\varepsilon_c = -D_c \left(1 - \phi_0 \right) \tag{3}$$

Previously, it was found that ϕ_c increases after CO₂ exposure, influenced by the synergistic effects of CO₂ pressure and reservoir temperature (Yang et al., 2023, 2024). There is a quantitative relationship between D_c and CO₂ pressure and temperature, which can be expressed as:

$$D_c = \frac{a_c p + b_c T + c_c - \phi_0}{1 - \phi_0} \tag{4}$$

where a_c , b_c and c_c can be calculated according to the variation law of shale porosity under different CO₂ pressures and temperatures (Yang et al., 2023); p represents the gas pressure; T is the gas temperature.

2.1.2 Mechanical weakening of shale

Chemical dissolution can deteriorate the mechanical characteristics of shale, and the damage degrees of elastic modulus (D_E) and Poisson's ratio (D_v) are defined to analyze the mechanical weakening degrees (Zhou et al., 2022):

$$D_{E} = 1 - \frac{E_{c}}{E_{0}}$$

$$D_{v} = 1 - \frac{v_{c}}{v_{0}}$$
(5)

where E_0 and v_0 denote the initial elastic modulus and Poisson's ratio, respectively, and E_c and v_c are the corresponding values after dissolution effect. The mechanical weakening was discovered to be further influenced by variations in CO_2 pressure and temperature (Yang et al., 2023), and its D_E and D_v can be expressed as:

$$D_E = d_c p + e_c T + f_c \tag{6}$$

$$D_{v} = g_{c}p + h_{c}T + i_{c} \tag{7}$$

where d_c , e_c , f_c , g_c , h_c , and i_c can be derived from the changes in E_c and v_c with varying CO₂ pressure and temperature conditions (Yang et al., 2023). By substituting Eqs. (6) and (7) into Eq. (5), E_c and v_c can be expressed as:

$$E_c = E_0 (1 - d_c p + e_c T + f_c)$$

$$v_c = v_0 (1 - g_c p + h_c T + i_c)$$
(8)

Substituting Eq. (8) into the shale deformation equation quantitatively characterizes the deformation resulting from the mechanical weakening of shale.

2.2 Governing equation of shale deformation

The primary factors that influence shale deformation are as follows: 1) Deformation caused by changes in effective stress (Kuang et al., 2024); 2) deformation caused by competitive adsorption-induced swelling (Wang et al., 2025); 3) defor-

mation caused by thermal expansion (Zhao et al., 2020a); 4) deformation caused by chemical dissolution. The shale strain

can be expressed as:

$$\varepsilon_{ij} = \frac{1}{2G}\sigma_{ij} - \left(\frac{1}{6G} - \frac{1}{9K}\right)\sigma_{kk}\delta_{ij} + \frac{\alpha}{3K}p_f\delta_{ij} + \frac{\beta}{3K}p_m\delta_{ij} + \frac{1}{3}\sum_{k=1}^2 \frac{\varepsilon_{L,k}b_kp_{mk}}{1 + \sum_{k=1}^2 b_kp_{mk}}\delta_{ij} + \frac{1}{3}\alpha_T T\delta_{ij} + \frac{\varepsilon_c}{3}\delta_{ij}$$
(9)

where ε_{ij} denotes the total strain tensor; σ_{ij} denotes the total stress; G and K are the shear modulus and bulk modulus, respectively, $G = E_c/2(1+v_c)$, $K = E_c/3(1-2v_c)$; σ_{kk} denotes the volumetric stress; δ_{ij} denotes the Kronecker delta function $((i = j, \delta_{ij} = 1; i \neq j, \delta_{ij} = 0)); p_m \text{ and } p_f \text{ denote the total}$ pressure in the matrix and fracture respectively; α and β are the Biot coefficients, $\alpha = 1 - K/K_s$, $\beta = 1 - K/(K_n \times a)$; a denotes the size of matrix; K_s denotes the skeleton bulk modulus; K_n denotes the fracture stiffness; α_T is a thermal expansion coefficient; $\mathcal{E}_{L,k}$ and b_k represent the maximum adsorption strain and Langmuir coefficient, respectively; the subscript k represents CH₄ (k = 1) and CO₂ (k = 2), respectively; ε_c is the shale strain caused by chemical dissolution effect.

By substituting Eq. (3) into (9), the equation that governs shale deformation can be obtained:

$$Gu_{i,jj} + \frac{G}{1 - 2\nu}u_{j,ji} - (\alpha + K \cdot A)p_{m1,i} - (\alpha + K \cdot B - aK)p_{m2,i} - \beta p_{f1,i} - (\beta - a_cK)p_{f2,i} - K(\alpha_T - b_c)T_{,i} + F_i = 0$$
 (10)

where F_i denotes the volume force in the *i*-direction; u_{ij} and u_{ii} denote the displacement component in the *i*-direction and j-direction; p_{m1} and p_{m2} denote the pressure of CH₄ and CO₂ in the matrix, respectively; A and B can be expressed as:

$$A = \frac{\varepsilon_{L,1}b_1(1+b_2p_{m2})}{(1+b_1p_{m1}+b_2p_{m2})^2} - \frac{\varepsilon_{L,2}b_1b_2p_{m2}}{(1+b_1p_{m1}+b_2p_{m2})^2}$$
(11)
$$B = \frac{\varepsilon_{L,2}b_2(1+b_1p_{m1})}{(1+b_1p_{m1}+b_2p_{m2})^2} - \frac{\varepsilon_{L,1}b_1b_2p_{m1}}{(1+b_1p_{m1}+b_2p_{m2})^2}$$
(12)

$$B = \frac{\varepsilon_{L,2}b_2(1 + b_1p_{m1})}{(1 + b_1p_{m1} + b_2p_{m2})^2} - \frac{\varepsilon_{L,1}b_1b_2p_{m1}}{(1 + b_1p_{m1} + b_2p_{m2})^2}$$
(12)

2.3 Governing equation of binary gas transport

2.3.1 Porosity and Permeability Model

It is assumed that shale is an ideal fracture body composed of matrix and fracture networks (Liu et al., 2021; Kuang et al., 2024). In this dual-pore system, a and b represent the size of matrix and fracture, respectively. The matrix volumetric strain (ε_m) , which incorporates the impacts of effective stress, competitive adsorption, thermal expansion, and chemical dissolution on shale deformation, is given using Eq. (9):

$$\varepsilon_{m} = \varepsilon_{e} + \varepsilon_{s} + \varepsilon_{T} + \varepsilon_{c} =
- \frac{\Delta \sigma_{m}}{K_{m}} + \frac{\varepsilon_{L,1} p_{m1} b_{1} + \varepsilon_{L,2} p_{m2} b_{2}}{1 + b_{1} p_{m1} + b_{2} p_{m2}}
+ \alpha_{T} \Delta T - D_{c} (1 - \phi_{0})$$
(13)

where ε_e , ε_s , ε_T , and ε_c represent the matrix strains caused by effective stress, competitive adsorption deformation, thermal expansion, and chemical dissolution effects, respectively; σ_m represents the effective stress applied to the matrix; K_m represents the matrix stiffness.

Both fracture and matrix contribute to the strain of shale bulk (Wu et al., 2011), that is:

$$\varepsilon_{v} = -\frac{b}{a}\varepsilon_{f} + \varepsilon_{m} \tag{14}$$

where ε_{v} and ε_{f} represent the volumetric strains of shale bulk and fractures, respectively.

Considering the influence of stress on shale fracture strain, assuming $\Delta \sigma_m = \Delta \sigma_f$, the following relationship is derived by substituting Eq. (13) into (14):

$$\varepsilon_{\nu} = -\left(\frac{b_0}{aK_f} + \frac{1}{K_m}\right) \Delta \sigma_m + \frac{\varepsilon_{L,1} p_{m1} b_1 + \varepsilon_{L,2} p_{m2} b_2}{1 + b_1 p_{m1} + b_2 p_{m2}} + \alpha_T \Delta T - D_c (1 - \phi_0)$$
(15)

where σ_f denotes the effective stress applied to the fracture; K_f denotes the fracture stiffness; b_0 denotes the initial size of fracture. Let $b_0/aK_f + 1/K_m = N$, then Eq. (15) can be

$$\Delta \sigma_m = N^{-1} \left[\frac{\varepsilon_{L,1} p_{m1} b_1 + \varepsilon_{L,2} p_{m2} b_2}{1 + b_1 p_{m1} + b_2 p_{m2}} + \alpha_T \Delta T - D_c (1 - \phi_0) - \varepsilon_v \right]$$
(16)

Then, the porosity (ϕ_m) of the shale matrix is differentiated to (Yuan et al., 2019):

$$d\phi_m = d\left(\frac{V_p}{V_m}\right) = \frac{dV_p}{V_m} - \frac{V_p}{V_m^2} dV = \frac{V_p}{V_m} \left(\frac{dV_p}{V_p} - \frac{dV_m}{V_m}\right)$$

$$= \phi_m \left(\varepsilon_m - \varepsilon_p\right)$$
(17)

where V_m and V_p represent shale matrix volume and pore volume, respectively; ε_m and pore volumetric strain (ε_p) can be expressed as:

$$\varepsilon_{m} = \left(1 - \frac{1}{NK_{m}}\right) \left[\frac{\varepsilon_{L,1}p_{m1}b_{1} + \varepsilon_{L,2}p_{m2}b_{2}}{1 + b_{1}p_{m1} + b_{2}p_{m2}} + \alpha_{T}\Delta T - D_{c}(1 - \phi_{0})\right] + \frac{1}{NK_{m}}\varepsilon_{v}$$

$$(18)$$

$$\varepsilon_{p} = \left(1 - \frac{1}{NK_{p}}\right) \left[\frac{\varepsilon_{L,1}p_{m1}b_{1} + \varepsilon_{L,2}p_{m2}b_{2}}{1 + b_{1}p_{m1} + b_{2}p_{m2}} + \alpha_{T}\Delta T - D_{c}(1 - \phi_{0})\right] + \frac{1}{NK_{p}}\varepsilon_{v}$$
(19)

where K_p is the modulus of pores.

Substituting Eqs. (18) and (19) into Eq. (17), the porosity model of shale matrix is obtained:

$$\phi_{m} = \phi_{m0} - \frac{\alpha}{K_{m}N} \left[\frac{\varepsilon_{L,1} p_{m1} b_{1} + \varepsilon_{L,2} p_{m2} b_{2}}{1 + b_{1} p_{m1} + b_{2} p_{m2}} + \alpha_{T} \Delta T - D_{c} (1 - \phi_{0}) - \varepsilon_{v} \right]$$
(20)

where ϕ_{m0} denotes the initial matrix porosity.

If shale is assumed to have a dual-porosity structure, the initial porosity (ϕ_0) and fracture porosity (ϕ_{f0}) can be obtained (Wang et al., 2025):

$$\phi_{f_0} = \frac{(a+b)^3 - a^3}{(a+b)^3} \approx \frac{3b_0}{a_0}$$
 (21)

$$\phi_f = \phi_{r_0} + \Delta \phi_f \approx \phi_{r_0} \left(1 + \frac{\Delta b}{b_0} \right) \tag{22}$$

Next, the ε_f can be obtained (Wu et al., 2011):

$$\frac{\Delta b}{b_0} = -\frac{\Delta \sigma_f}{K_f} = -\frac{\Delta \sigma_m}{K_f} \tag{23}$$

By substituting Eqs. (16) and (23) into Eq. (22), the porosity model of shale fractures can be obtained:

$$\phi_{f} = \phi_{f_{0}} - \frac{\phi_{f_{0}}}{K_{f}N} \left[\frac{\varepsilon_{L,1}p_{m1}b_{1} + \varepsilon_{L,2}p_{m2}b_{2}}{1 + b_{1}p_{m1} + b_{2}p_{m2}} + \alpha_{T}\Delta T - D_{c}(1 - \phi_{0}) - \varepsilon_{v} \right]$$
(24)

Combined with Eqs. (20) and (24), according to the cubic law (Wang et al., 2025), the permeability of matrix (k_m) and fractures (k_f) within shale can be obtained:

$$k_{m} = k_{m0} \left\{ 1 - \frac{\alpha}{K_{m}N\phi_{m0}} \left[\frac{\varepsilon_{L,1}p_{m1}b_{1} + \varepsilon_{L,2}p_{m2}b_{2}}{1 + b_{1}p_{m1} + b_{2}p_{m2}} + \alpha_{T}\Delta T - D_{c}(1 - \phi_{0}) - \varepsilon_{v} \right] \right\}^{3}$$
(25)

$$k_{f} = k_{f0} \left\{ 1 - \frac{1}{K_{f}N} \left[\frac{\varepsilon_{L,1} p_{m1} b_{1} + \varepsilon_{L,2} p_{m2} b_{2}}{1 + b_{1} p_{m1} + b_{2} p_{m2}} + \alpha_{T} \Delta T - D_{c} (1 - \phi_{0}) - \varepsilon_{v} \right] \right\}^{3}$$
(26)

where k_m and k_{m0} represent shale matrix permeability and initial matrix permeability, respectively; k_f and k_{f0} denote shale fracture permeability and initial fracture permeability, respectively.

2.3.2 Gas transport in shale matrix

Given that flow within the shale matrix is primarily diffusive, the mass balance equation is derived from the principle of mass conservation (Zhao et al., 2020a):

$$\frac{\partial (m_{mk})}{\partial t} - \nabla \cdot (D_k \nabla m_{mk}) = \frac{M_k K_v}{RT} (p_{fk} - p_{mk})$$
 (27)

where D_k denotes the diffusion coefficient of k-component gas; K_v denotes the material exchange rate of k-component gas; R denotes the gas molar constant; t denotes time; M_k denotes the molar mass of k-component gas; m_{mk} denotes the gas content of k-component gas, which can be obtained as (Kuang et al., 2024):

$$m_{mk} = \frac{p_{mk}\phi_m M_k}{RT} + \rho_c \rho_{3k} \frac{V_{L,k}b_k p_{mk}}{1 + p_{m1}b_1 + p_{m2}b_2}$$
 where ρ_c and ρ_{sk} represent the density of shale and k -

where ρ_c and ρ_{sk} represent the density of shale and k-component gas in the standard state, respectively; $V_{L,k}$ is the maximum adsorption volume of k-component gas in shale.

The partial differential equation governing CH_4 and CO_2 flow in the matrix is derived by substituting Eq. (28) into Eq. (27):

$$M_{1}\left(p_{m1}\frac{\partial\phi_{m}}{\partial t}+\phi_{m}\frac{\partial p_{m1}}{\partial t}\right)+C_{C1}\frac{\partial p_{m1}}{\partial t}-D_{D1}\frac{\partial p_{m2}}{\partial t}$$

$$-\nabla\cdot D_{1}\left(M_{1}\phi_{m}\nabla p_{m1}+C_{C1}\nabla p_{m1}-D_{D1}\nabla p_{m2}\right)$$

$$=M_{1}K_{v}\left(p_{f1}-p_{m1}\right)$$

$$M_{2}\left(p_{m2}\frac{\partial\phi_{m}}{\partial t}+\phi_{m}\frac{\partial p_{m2}}{\partial t}\right)+C_{C2}\frac{\partial p_{m2}}{\partial t}-D_{D2}\frac{\partial p_{m1}}{\partial t}$$

$$-\nabla\cdot D_{2}\left(M_{2}\phi_{m}\nabla p_{m2}+C_{C2}\nabla p_{m2}-D_{D2}\nabla p_{m1}\right)$$

$$=M_{2}K_{v}\left(p_{f2}-p_{m2}\right)$$

$$(29)$$

where C_{C1} , C_{C2} , D_{D1} , D_{D2} are the component terms of the derivative form of the adsorbed gas content model in shale, which can be expressed as:

$$C_{C1} = \rho_c \rho_{s1} \frac{V_{L,1} b_1 (1 + p_{m2} b_2)}{(1 + p_{m1} b_1 + p_{m2} b_2)^2}$$

$$C_{C2} = \rho_c \rho_{s2} \frac{V_{L,2} b_2 (1 + p_{m1} b_1)}{(1 + p_{m1} b_1 + p_{m2} b_2)^2}$$

$$D_{D1} = \rho_c \rho_{s1} \frac{V_{L,1} b_1 p_{m1} b_2}{(1 + p_{m1} b_1 + p_{m2} b_2)^2}$$

$$D_{D2} = \rho_c \rho_{s2} \frac{V_{L,2} b_2 p_{m2} b_1}{(1 + p_{m1} b_1 + p_{m2} b_2)^2}$$
(31)

The continuity equations for binary gas flow within the matrix can be derived by substituting Eq. (20) into Eqs. (29) and (30):

$$\left(M_{i}\phi_{m}+C_{Ci}-\frac{M_{i}p_{mi}\alpha A}{RTK_{m}N}\right)\frac{\partial p_{mi}}{\partial t}-\left[D_{Di}+\frac{M_{i}p_{mi}\alpha(B-a_{c}RT)}{RTK_{m}N}\right]\frac{\partial p_{mj}}{\partial t}-\left[\frac{M_{i}p_{mi}\alpha(RT\alpha_{T}-a_{c}Rp_{mj}-RTb_{c})}{RTK_{m}N}\right]\frac{\partial T}{\partial t} + \frac{M_{i}p_{mi}\alpha}{K_{m}N}\frac{\partial \varepsilon_{v}}{\partial t}-\nabla \cdot D_{i}\left[(M_{i}\phi_{m}+C_{Ci})\nabla p_{mi}-D_{Di}\nabla p_{mj}\right]=M_{i}K_{v}(p_{fi}-p_{mi})$$
(32)

2.3.3 Gas transport in shale fracture

Considering that flow within the shale fractures primarily occurs in the form of Darcy flow, and the gas mainly exists in a free state, the mass balance equation within shale fractures can be obtained (Zhao et al., 2020a):

$$\frac{\partial(m_{fk})}{\partial t} + \nabla \cdot (\rho_{fk}\nu_k) = \frac{M_k K_{\nu}}{RT} (p_{mk} - p_{fk})$$
 (33)

where ρ_{fk} denotes the *k*-component gas density within the fracture; v_k denotes the *k*-component gas flow rate within the fracture; m_{fk} denotes the *k*-component gas content within the fracture and is defined as (Kuang et al., 2024):

$$m_{fk} = \frac{p_{fk}\phi_f M_k}{RT} \tag{34}$$

The flow in the fracture is mainly in the form of Darcy flow, and its flow velocity v_k can be obtained (Zhao et al., 2023):

$$v_k = -\frac{k_f}{\mu_k} \cdot \nabla p_{fk} \tag{35}$$

where μ_k represents the dynamic viscosity of k-component

gas.

Combined with the Eqs. (33)-(35), the flow of CH₄ and CO₂ within the fracture is governed by the following partial differential equations:

$$p_{f1}\frac{\partial \phi_{f}}{\partial t} + \phi_{f}\frac{\partial p_{f1}}{\partial t} - \nabla \cdot \left[p_{f1} \cdot \frac{k_{f}}{\mu_{1}} \cdot \nabla p_{f1}\right] = K_{v}(p_{m1} - p_{f1})$$

$$(36)$$

$$p_{f2}\frac{\partial \phi_{f}}{\partial t} + \phi_{f}\frac{\partial p_{f2}}{\partial t} - \nabla \cdot \left[p_{f2} \cdot \frac{k_{f}}{\mu_{2}} \cdot \nabla p_{f2}\right] = K_{v}(p_{m2} - p_{f2})$$

$$(37)$$

Substituting Eq. (24) into Eqs. (36) and (37), the continuity equation governing flow in shale fractures can be obtained:

$$M_{i}\phi_{f}\frac{\partial p_{fi}}{\partial t} + \frac{M_{i}p_{fi}\phi_{f0}}{K_{f}N}\frac{\partial \varepsilon_{v}}{\partial t} - \frac{M_{i}p_{fi}\phi_{f0}A}{RTK_{f}N}\frac{\partial p_{mi}}{\partial t} - \frac{M_{i}p_{fi}\phi_{f0}(B - a_{c}RT)}{RTK_{f}N}\frac{\partial p_{mj}}{\partial t} - \frac{M_{i}p_{fi}\phi_{f0}(RT\alpha_{T} - a_{c}Rp_{mj} - RTb_{c})}{RTK_{f}N}\frac{\partial T}{\partial t} - \nabla \cdot \left[M_{i}p_{fi}\cdot\frac{k_{f}}{u_{i}}\cdot\nabla p_{fi}\right] = M_{i}K_{v}(p_{mi} - p_{fi})$$
(38)

2.4 Governing equation of thermal field

It is assumed that the shale system satisfies the thermal equilibrium state. In the reservoir injected with CO₂, the internal energy change, the strain energy of shale, the heat conduction, and convection will all produce energy exchange, which can be given by (Liu et al., 2021):

$$\frac{\partial (C_e T)}{\partial t} + \eta_e \nabla T - \nabla \cdot (\lambda_e \nabla T) + K \alpha_T T \frac{\partial \varepsilon_v}{\partial t} = 0$$
 (39)

where C_e represents the effective specific heat constant; λ_e denotes the heat conductivity coefficient; η_e is the heat convection coefficient, C_e , η_e and λ_e can be respectively defined as (Liu et al., 2021):

$$C_e = (1 - \phi_m - \phi_f) \rho_c C_c + \sum_{k=1}^{2} (\phi_f \rho_{fk} C_{gk} + \phi_m \rho_{mk} C_{gk})$$
 (40)

$$\eta_e = -\sum_{k=1}^2 \frac{\rho_{fk} C_{gk} k_f}{\mu_k} \nabla p_{fk} \tag{41}$$

$$\lambda_e = (1 - \phi_m - \phi_f) \lambda_s + (\phi_m + \phi_f) \lambda_g \tag{42}$$

where C_c denotes the specific heat constant; C_{gk} denotes the specific heat constant under k-component gas, λ_s and λ_g are the heat conductivity coefficient of reservoir and gas respectively; ρ_{mk} denotes the k-component gas density within matrix.

2.5 Multifield coupling

By combining Eqs. (10), (32), (38) and (39), the THMC coupling equations incorporating mechanical weakening effects for CO₂-ESGR are derived. The impacts of effective stress, competitive adsorption, thermal expansion, chemical dissolution, mechanical weakening, and other factors on shale porosity and permeability are comprehensively considered (Eq. (20) and Eqs. (24)-(26)), with the coupling relationship illustrated in Fig. 1.

The numerical solution of the above equations is computationally addressed via the Solid Mechanics and PDE modules in COMSOL Multiphysics software. Utilizing the finite element method, the software facilitates the simulation of coupled multiphysics processes.

3. Model verifications

To validate the effectiveness of the fully coupled model, cylindrical shale sample was used to conduct CO₂-CH₄ displacement tests, and a comparison was performed between the experimental and simulation results. The test sample was collected from the Wufeng Formation in the Sichuan Basin and machined into cylindrical sample with dimensions of 100 mm in diameter and 200 mm in height. To simulate the CO₂-ESGR processes, a circular hole was drilled along the center end face of the sample as the wellbore. After processing, fracturing pipes were inserted and sealed with a blend of epoxy resin and hardener. Displacement tests were performed using a self-developed experimental setup (Zhou et al., 2016). The shale sample was first saturated with CH₄ under stress conditions, followed by constant-pressure CO₂ injection, to quantitatively measure the outlet flow rate and variations in gas molar composition at the opposite end of the sample. The initial conditions were set as follows: CH₄ pressure at 5 MPa, CO₂ injection pressure at 9 MPa, and axial/confining pressures at 15 MPa, with a constant temperature of 338 K.

The numerical simulation employed consistent experimental conditions as the model's boundary conditions. Given the assumption of isotropy and homogeneity in the shale sample, a two-dimensional simplification of the model was adopted (Li and Elsworth, 2019). The model dimensions exactly matched the diameter and height of cylindrical samples. A schematic diagram of model geometry and boundary conditions is presented in Fig. S2 (Supplementary file). The initial temperature of the shale sample was set at 338 K. The sample was subjected to a constant 15 MPa stress on its top and sides. A CO₂ pressure of 9 MPa was maintained at the bottom surface and the fracturing holes, with an initial condition of zero CH₄ presence. The shale sample interior maintained a CH₄ pressure of 5 MPa with no CO₂ present. Zero-flux boundary conditions were imposed at both ends, while atmospheric pressure was set for the top surface. The parameters used in the model are presented in Table S1 (Supplementary file), and the key physical parameters of the shale were independently measured

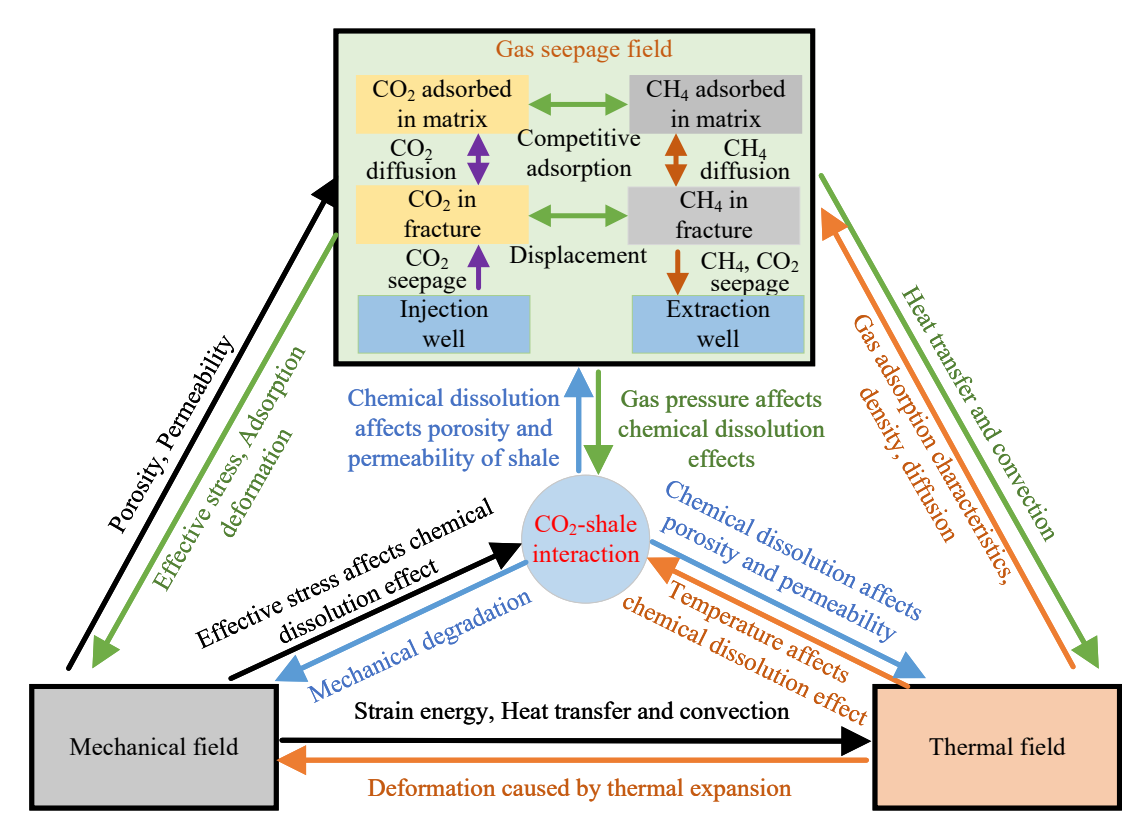


Fig. 1. THMC coupling relationship in the CO₂-ESGR process.

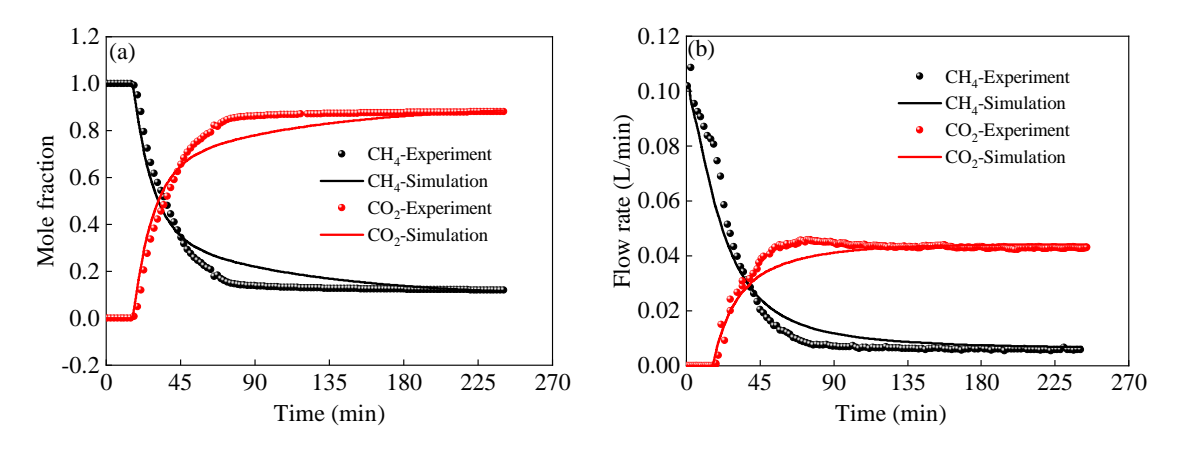


Fig. 2. Verification of results of simulation and experiment: (a) Mole fraction and (b) flow rate.

prior to laboratory testing.

To validate the numerical model, a comparison between the simulation results and experimental data was conducted (Fig. 2). The simulation results can generally well represent the trends of the molar ratio and flow rate changes of CH₄ and CO₂, which validates the applicability of the proposed model. It should be noted that some deviations occurred between the simulation results and the experimental results during the middle stage of CO₂ displacement. The analysis suggested that this is mainly due to the errors caused by the adsorption parameters of CH₄ and CO₂ within the shale matrix, which were calculated based on the results of isothermal adsorption experiments conducted on powder samples. Compared with

cylindrical samples, powder samples have a larger specific surface area and are not subject to external stress, so their adsorption capacity is stronger. Therefore, this deviation leads to the overestimation of shale adsorption capacity. Du et al., 2019 asserted that the adsorption of gases in shale causes the breakthrough curves of CO₂ and CH₄ to be asymmetric with a long tail. Due to the deviations in this shale adsorption test, the tailing phenomenon of the calculated breakthrough curves was more pronounced, and the time for the molar ratio and flow rate values to reach the inflection point was prolonged. However, this did not affect the final values of CH₄ and CO₂ after they reached equilibrium.

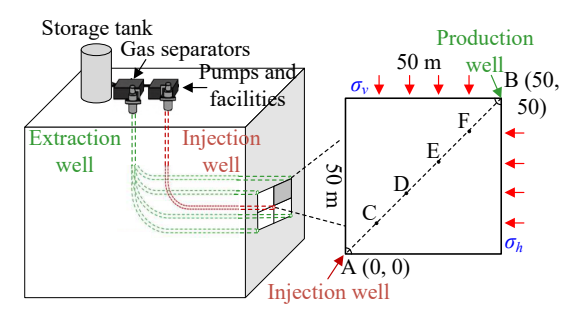


Fig. 3. Schematic diagram of well distribution and simulation geometric model.

4. Numerical simulation on CO₂-ESGR

4.1 Simulation case

To investigate the flow evolution of binary gas during CO₂-ESGR and to evaluate CH₄ production and CO₂ storage under various factors, the study area located in the northeastern Sichuan Basin was investigated using a fully coupled model for numerical simulations. A completed exploration well (Well WQ2) in this study area was selected for analysis. The exploration well results (Zhao et al., 2020a; Liu et al., 2021) showed that the area has huge potential for shale gas production. The simulation model for the target layer of Wufeng formation shale (burial depth: 1,200-1,300 m, thickness: 100 m) utilized a standard five-point pattern, featuring one injection well and four corner production wells with an axisymmetric geometry (Li and Elsworth, 2019; Liu et al., 2021). In this simulation, a two-dimensional cross-section was selected, incorporating the symmetry of the model, and one-quarter of the study area was simulated (Fig. 3).

The model size was 50×50 m², with a well radius of 0.1 m, according to the logging curve of WQ2 well (Zhao et al., 2020a; Liu et al., 2021), the boundary conditions were as follows: (1) The *in-situ* stress magnitudes were 30 MPa in the horizontal direction (σ_h) and 36 MPa in the vertical direction (σ_{ν}) . Therefore, the stress was set to 30 and 36 MPa at the right and upper ends of the shale reservoir, respectively, and the roller support was set at the bottom and left ends of the reservoir. (2) Based on the burial depth of shale reservoir and the pressure gradient in the Sichuan Basin (Yin et al., 2016), the shale reservoir was initialized with a CH₄ pressure of 8 MPa. Both the injection and production wells had a radius of 0.1 m, with the former located in the bottom-left corner and the latter in the top-right corner of the model. The injection CO₂ pressure in the injection well was set to 10 MPa. Constantpressure production was assigned to the production well, with the outlet pressure set to atmospheric pressure. To isolate the study area and eliminate interference from far-field fluid exchange, all other model boundaries except the injection well and production well were defined as zero-flux boundaries. (3) The model's thermal boundary conditions were defined with an initial reservoir temperature of 309 K and an injection temperature of 323 K for CO₂ in injection well. To isolate the system and accurately model the thermal effects of CO₂ injection and its interaction with shale, all other external boundaries were specified as thermally insulated, designed to preclude any heat exchange with the surroundings.

The parameters for this simulation, detailed in Table S2 (Supplementary file), were primarily based on field test data from the study area and references (Zhao et al., 2020a; Liu et al., 2021). The target reservoir formation selected for this simulation was consistent with that investigated in these referenced studies. Zhao et al. (2020a) and Liu et al. (2021) conducted detailed characterizations of this specific reservoir and measured its key physical properties. The parameters for chemical dissolution and mechanical weakening were calculated from previous experimental studies, using shale from the Wufeng Formation in the Sichuan Basin (Yang et al., 2023, 2024). The simulation duration was set to 10,000 days, with intercept line AB and observation points C (10,10), D (20,20), E (30,30), and F (40,40) added to monitor the shale reservoir parameters at these points.

4.2 Evolution of shale reservoir parameters

To reveal the evolution of reservoir parameters during CO_2 -ESGR processes, a conventional recovery group was added for comparison. This group was set to have no CO_2 injection, and the initial reservoir CH_4 pressure was 8 MPa. The reservoir parameters and boundary conditions were consistent with those under CO_2 injection conditions. Comparative analyses were performed on CH_4/CO_2 content variations, matrix/fracture permeability evolution, as well as CH_4 production and CO_2 storage under both scenarios.

(1) Permeability variation and gas concentration distribution

The variation in relative permeability in the shale matrix is shown in Fig. 4(a). For conventional recovery without CO₂ injection, the relative permeability at each monitoring point within the shale matrix exhibits an increasing trend over time, with more pronounced variations observed at points closer to the production well. This phenomenon is primarily driven by the progressive desorption of matrix-adsorbed CH₄ following the gradual displacement of free CH₄ from the fractures. The resultant matrix shrinkage leads to a subsequent increase in the pore size of the matrix, which in turn results in higher permeability (Zhou et al., 2022). The closer to the production well, the faster the rate of discharge and desorption of CH₄, and thus the rate of increase in permeability is also correspondingly higher. For CO₂ enhanced recovery, the relative permeability at each monitoring point within the shale matrix initially increases rapidly and then gradually decreases over time. A rapid increase in CO₂ pressure occurs during the initial injection period into the shale reservoir, and the chemical dissolution effect and the effective stress effect gradually strengthen (Yang et al., 2024), causing a rapid increase in the shale matrix's relative permeability. However, as the injection time progresses, the adsorption-induced swelling effect of shale on CO₂ gradually becomes dominant (Khosravi et al., 2023). Simultaneously, the chemical dissolution effect of CO₂ progressively weakens the mechanical characteristics of shale, resulting in a gradual reduction of the elastic modulus and an increase in Poisson's ratio (Yang et al., 2023). Consequently, a rapid decrease in the matrix permeability occurs as

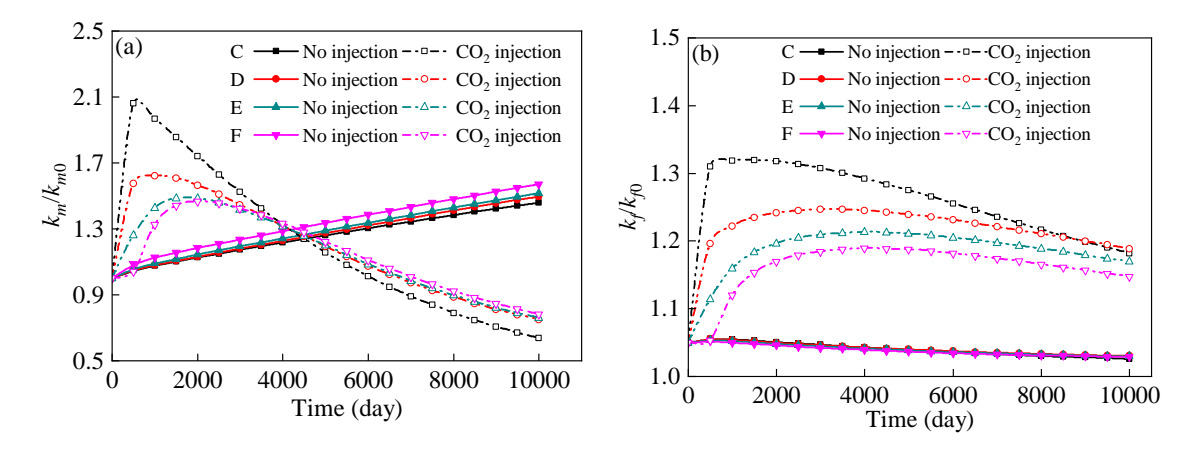


Fig. 4. Relative permeability variation in shale reservoir during conventional recovery and CO₂ enhanced recovery for (a) shale matrix and (b) fracture.

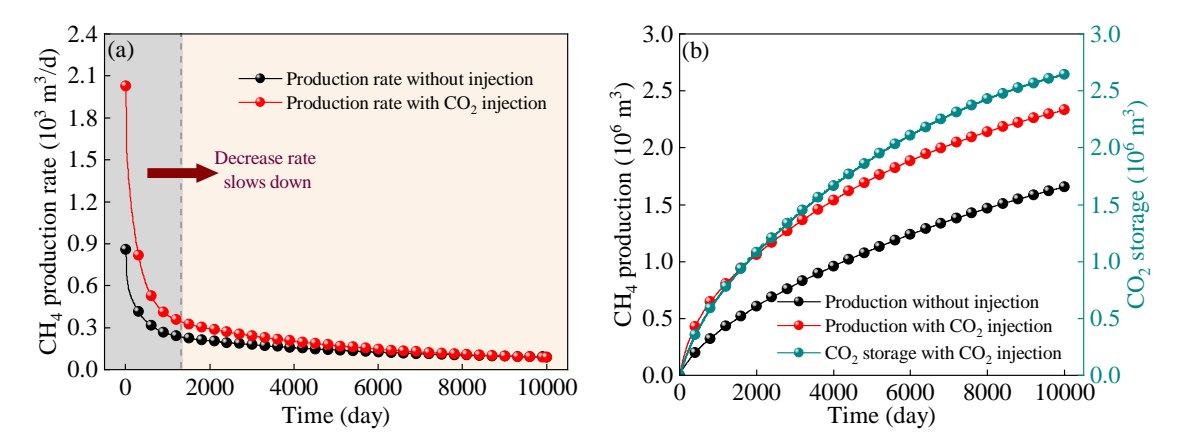


Fig. 5. (a) CH₄ production rate, (b) CH₄ production and CO₂ storage of shale reservoir during conventional recovery and CO₂ enhanced recovery.

a result of additional pore compression under the same stress state (Yang et al., 2022).

The variation in relative permeability in the shale fractures is shown in Fig. 4(b). For conventional recovery without CO₂ injection, the relative permeability at each monitoring point within the shale fractures initially increases and then gradually decreases over time. During the initial period, matrix desorption-induced shrinkage plays a dominant role, while during the middle to late periods, as CH₄ is discharged, the shale fractures gradually compress under reservoir stress, leading to a gradual reduction in fracture permeability. For CO₂ enhanced recovery, the relative permeability within the shale fractures also shows an initial rapid increase, followed by a gradual decrease over time. This change is a result of the coupling influences of chemical dissolution, effective stress, mechanical weakening, and differential swelling. Due to elevated CO₂ pressure around the injection well, relative permeability varies more markedly in these regions, which intensifies the chemical dissolution and effective stress effects, causing a rapid increase in permeability near the gas injection point.

Furthermore, a comparative analysis of CH₄ and CO₂

concentration distribution was conducted to evaluate the performance of the CO₂ enhanced recovery method, and the results are presented in Appendix B (Supplementary file).

(2) CH₄ recovery and CO₂ storage

The dynamic interplay between the gas production rate, CH₄ production and CO₂ storage is critical for evaluating the process efficiency. This relationship is detailed in Fig. 5. CO₂ injection significantly increases CH₄ production, with cumulative gas exhibiting rapid initial growth that gradually slows. Within 10,000 days, the CH₄ production under conventional recovery is 1.65×10^6 m³, and it is 2.33×10^6 m³ under CO₂ enhanced recovery, with an increase of 40.70%. Defining CH₄ recovery efficiency as the ratio of CH₄ production to the initial reservoir content. After 100, 1,000, 5,000, and 10,000 days of production, the recovery efficiencies for conventional production are 1.85%, 10.93%, 31.81%, and 47.65%, respectively, while the recovery efficiencies for CO₂ enhanced recovery are 4.34%, 20.99%, 49.67%, and 67.04%, respectively, which indicating higher recovery efficiencies at all time intervals with CO₂ injection. In addition, the trend of CO₂ storage is consistent with that of CH₄ production. Within 10,000 days, the cumulative storage of CO₂ in shale reservoir reaches

Scheme	Reservoir stress (MPa)	Injection pressure (MPa)	Injection temperature (K)	Chemical effect
1	$\sigma_h, \sigma_v = 30, 36, 42$	10	323	
2	$\sigma_h, \sigma_v = 36$	10, 15, 20	323	With C-M effect
3	$\sigma_h, \sigma_v = 36$	10	323, 338, 353	
4	$\sigma_h, \sigma_v = 36$	15	323	With C-M effect, Without M effect, Without C-M effect
Decreased	I rapidly	6 MPa	1.45 (b) 1.35	Decreased slowly

Table 1. Simulation scheme of influencing factors.

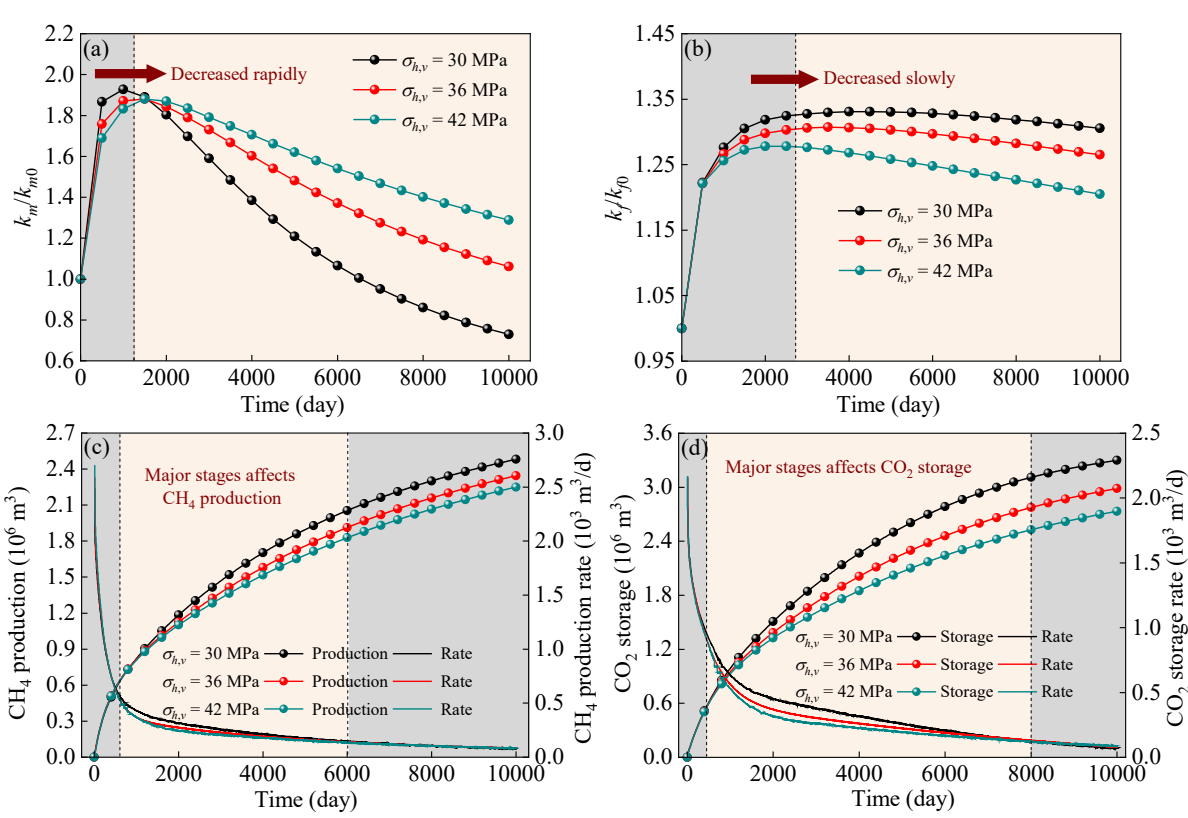


Fig. 6. Impact of reservoir stress on the shale reservoir's (point D) (a) matrix and (b) fracture permeability, (c) CH₄ production and (d) CO₂ storage.

 2.64×10^6 m³. The comprehensive results indicate that it is advantageous to carry out CO₂-ESGR in this reservoir.

4.3 Analysis of influencing factors during the CO₂-ESGR process

Multiple factors exert a combined influence on the efficiency of CO₂-ESGR. This work discusses the impact of reservoir stress, CO₂ injection pressure, injection temperature, and the chemical dissolution-mechanical weakening (C-M) effect. The sensitivity of individual factor influencing the CO₂-ESGR simulation results was evaluated using the control variable method. Table 1 is the simulation scheme of the influencing factors, and the initial CH₄ pressure is set at 8 MPa.

4.3.1 Reservoir stress

The monitoring point D was utilized to analyze the impact of reservoir stress on the permeability of shale matrix (Fig. 6(a)) and fractures (Fig. 6(b)). An initial increase followed by a gradual decrease in relative permeability was observed over time for both the shale matrix and fractures. For matrix permeability, a higher stress resulted in a lower rate of relative permeability increase in the shale matrix during the initial period of CO₂ injection, which indicates that high stress can inhibit the chemical dissolution effect. The matrix relative permeability during the middle and late injection periods decreased more rapidly under lower stress conditions, primarily due to the more pronounced adsorption-induced swelling effect in shale under such conditions (Zeng et al., 2023). For fracture permeability, the relative permeability of shale fracture during the initial injection period was higher under lower

stress conditions, primarily due to the coupling impacts of chemical dissolution and effective stress. The fracture relative permeability during the middle and late periods of injection decreased more rapidly under higher stress conditions, mainly due to the gradual dominance of mechanical weakening effect at this stage. The shale fractures were further compressed under high stress conditions, leading to a further decrease in permeability. In addition, the gas distribution within the reservoir is fundamentally controlled by reservoir stress conditions. Therefore, the impact of reservoir stress on gas concentration in shale reservoirs was further analyzed, and the results are presented in Appendix C (Supplementary file).

The impact of reservoir stress on CH₄ recovery and CO₂ storage are shown in Figs. 6(c) and 6(d). The results suggest that CH₄ production and CO₂ storage are lower under higher stress. Under different stress conditions (30, 36, 42 MPa), CH₄ production after 10,000 days was 2.48×10^6 , 2.34×10^6 , and 2.25×10^6 m³, respectively. The CO₂ storage capacity was 3.30×10^6 , 2.99×10^6 , and 2.73×10^6 m³, respectively. Combined with the permeability curve, it can be found that the inhibitory impact of stress on the efficiency of CO₂-ESGR is mainly during the middle period.

4.3.2 Injection pressure

The monitoring point D was utilized to analyze the impact of CO₂ injection pressure on the permeability of shale matrix (Fig. S3(a) in Supplementary file) and fractures (Fig. S3(b) in Supplementary file). The results show that, compared with the reservoir stress conditions, the relative permeability of shale has a more pronounced increasing trend with higher injection pressure during the initial injection period. The key mechanism is the enhanced dissolution effect on shale, driven by increased CO₂ injection pressure, triggering a substantial dissolution of both clay and carbonate minerals, thereby increasing shale porosity and pore size (Yang et al., 2022, 2023). The relative permeability of shale during the middle and late periods decreases more rapidly as the injection pressure increases, primarily caused by the coupling impacts of adsorption swelling and mechanical weakening. It is also observed that the relative permeability of fracture exhibits a smaller magnitude of change compared to that of the matrix, indicating that chemical effects and adsorption swelling have a more significant influence on the matrix permeability. Next, the impact of injection pressure on gas concentration in shale reservoirs was further analyzed, and the results are presented in Appendix C (Supplementary file).

The impact of CO_2 injection pressure on CH_4 recovery and CO_2 storage are shown in Figs. S3(c) and S3(d) in Supplementary file, respectively. The results suggest that the CH_4 production and CO_2 storage are higher under higher CO_2 pressure. Under different injection pressure conditions (10, 15, 20 MPa), the CH_4 production after 10,000 days was 2.34×10^6 , 2.46×10^6 and 2.88×10^6 m³, respectively, and the CO_2 storage capacity was 2.99×10^6 , 4.99×10^6 and 6.78×10^6 m³, respectively. It can be found that the impact of CO_2 injection pressure on the efficiency of CO_2 -ESGR is mainly during the initial and middle periods of injection.

4.3.3 Injection temperature

The monitoring point D was utilized to analyze the impact of injection temperature on the permeability of shale matrix (Fig. S4(a) in Supplementary file) and fractures (Fig. S4(b) in Supplementary file). The increase rate of the relative permeability of shale during the initial period of injection decreases as injection temperature increases. The chemical dissolution effect is strongly influenced by temperature, and previous studies have also found that the dissolution capacity of ScCO₂ on inorganic minerals in shale decreases as the temperature increases, resulting in a limited increase in shale porosity and pore size (Yang et al., 2022, 2023). When the injection time exceeds 2,000 days, the relative permeability of shale gradually decreases, the rate of which becomes higher as the injection temperature decreases, primarily caused by the gradual enhancement in the promoting effect of low temperature on the competitive adsorption and mechanical weakening effects during the middle and late periods, causing permeability to decrease rapidly. Next, the impact of injection temperature on gas concentration in shale reservoirs was further analyzed, and the results are presented in Appendix C (Supplementary file).

The impact of injection temperature on CH₄ recovery and CO₂ storage are shown in Figs. S4(c) and S4(d) in Supplementary file. The results suggest that lower injection temperature can significantly increase CH₄ production and CO₂ storage capacity. Under different temperature conditions (323, 338 and 353 K), the CH₄ production after 10,000 days was 2.34×10^6 , 2.22×10^6 and 2.07×10^6 m³, respectively, and the CO₂ storage capacity was 2.99×10^6 , 2.59×10^6 and 2.14×10^6 m³, respectively. Combined with the rate curve, it can be found that the impact of injection temperature on the efficiency of CO₂-ESGR is mainly during the initial and middle periods.

4.3.4 Chemical dissolution-mechanical weakening effect

The monitoring point C was selected to analyze the impact of C-M effect on the permeability of shale matrix (Fig. 7(a)) and fractures (Fig. 7(b)). The shale relative permeability calculated by the model incorporating the C-M effect and the model not incorporating the M effect both exhibits a consistent trend of initial increase, followed by subsequent decrease over time. In contrast, the relative permeability calculated by the model not incorporating the C-M effect shows a decreasing trend. These results indicate that chemical dissolution primarily enhances shale permeability, while mechanical weakening reduces it significantly. Compared to the effective stress effect, adsorption-induced swelling has a stronger impact on permeability. Next, the impact of C-M effect on gas concentration in shale reservoirs was further analyzed, and the results are presented in Appendix C (Supplementary file).

The impact of C-M effect on CH₄ recovery and CO₂ storage are shown in Figs. 7(c) and 7(d). In different situations (with C-M effect, without M effect, and without C-M effect), the CH₄ production after 10,000 days was 2.46×10^6 , 2.56×10^6 and 2.31×10^6 m³, respectively, and the CO₂ storage capacity was 4.98×10^6 , 4.71×10^6 and 4.46×10^6 m³, respectively. For CH₄ production, the CH₄ production

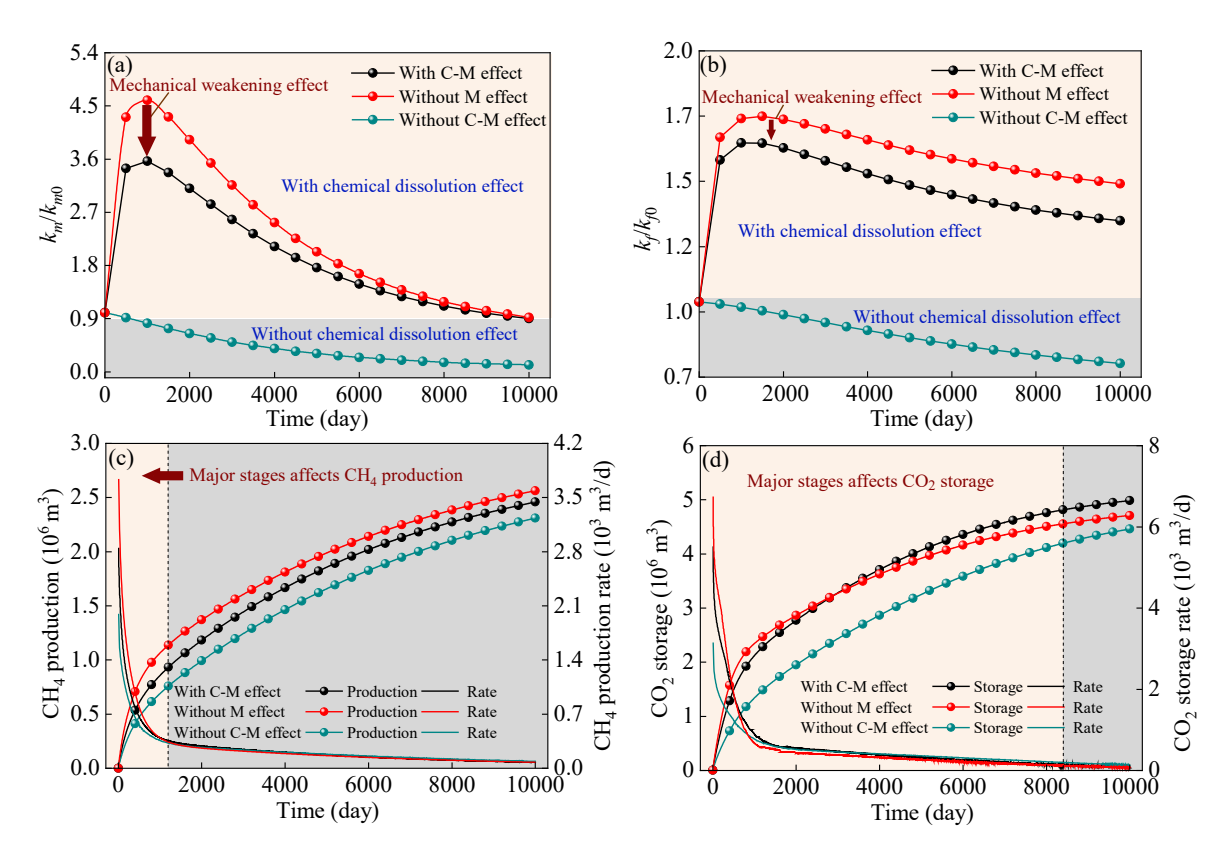


Fig. 7. Effect of chemical dissolution-mechanical weakening effect on the shale reservoir's (point C) (a) matrix and (b) fracture permeability, (c) CH₄ production, and (d) CO₂ storage.

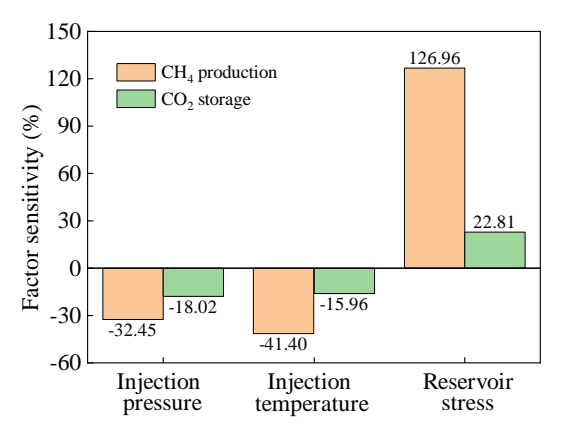


Fig. 8. Sensitivity analysis of various influencing factors.

calculated by the model without C-M effect and the model without M effect was significantly lower and higher than the calculation values incorporating the C-M effect, respectively. For CO₂ storage, the C-M effect model calculated the highest storage capacity.

4.3.5 Sensitivity analysis of various influencing factors

A sensitivity analysis was carried out for various influencing factors under chemical dissolution-mechanical weakening conditions, with the aim to determine the relative influence of key parameters on the simulation results, including the final values of CH₄ production and CO₂ storage. The sensitivity of these results is shown by a Tornado plot (Fig. 8). The baseline

parameters are set as reservoir stress = 36 MPa, injection pressure = 10 MPa, injection temperature = 323 K. The analysis of Fig. 8 reveals that when chemical dissolution-mechanical weakening coupling is considered, injection pressure emerges as the most influential parameter. Furthermore, reservoir stress demonstrates a greater impact on CH₄ production than injection temperature, whereas injection temperature exhibits a more pronounced effect on CO_2 storage compared to reservoir stress.

4.4 Implication for CO₂-ESGR

During the CO_2 -ESGR process, the injection of CO_2 into shale formations facilitates its transition to a supercritical state in the shale reservoir environment. As CO_2 is continuously injected, changes occur in the reservoir's THMC fields (Liu et al., 2021; Yang et al., 2022), further affecting the permeability characteristics of shale. In this work, it was found that effective stress, chemical dissolution, competitive adsorption, and mechanical weakening effects are all significant factors affecting the shale permeability.

The analysis of different influencing factors in the CO₂-ESGR process is shown in Fig. 9. Through simulation, it is found that during the initial injection period, the efficacy of CO₂-ESGR is predominantly governed by the effects of chemical dissolution and effective stress. To maximize both CH₄ displacement efficiency and CO₂ storage capacity during this phase, the implementation of elevated injection pressures coupled with moderately reduced injection temperatures is

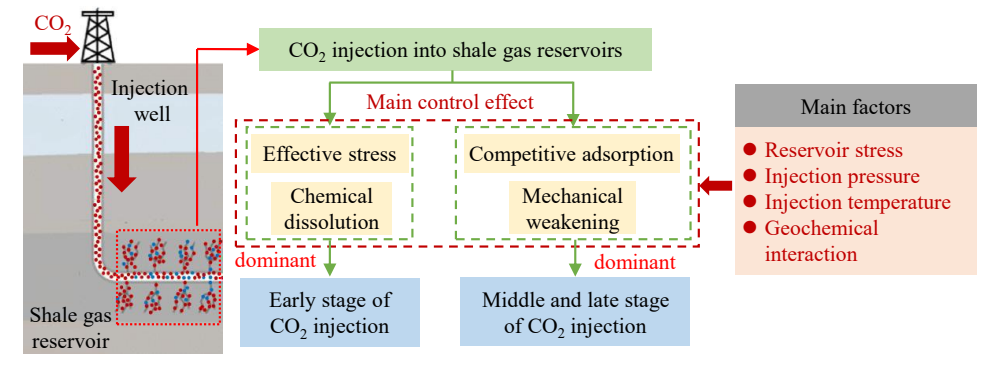


Fig. 9. Analysis of influencing factors during the CO₂-ESGR process.

recommended. Through this combination, CO₂ density is enhanced and displacement efficiency is improved while favorable conditions for chemical interactions are maintained. During the middle and late injection periods, the competitive adsorption and mechanical weakening effects are increasingly dominated. Excessively high injection pressures should be avoided, since permeability reduction may be accelerated through enhanced mechanical compression. Instead, a controlled pressure reduction strategy with moderate temperature maintenance is demonstrated to be more effective for sustaining long-term injectivity.

Furthermore, it is emphasized that the consideration of CO₂-shale chemical interactions throughout the entire project lifecycle is crucial. These simulation insights, derived from the coupled THMC model, provide a scientific basis for designing efficient and sustainable CO₂-ESGR field implementations.

5. Conclusions

To analyze coupling relationships and identify the main control factors in the CO₂-ESGR process, this paper presents a fully coupled THMC model that incorporates mechanical weakening. Main findings include:

- As the production time progresses, the permeability of shale matrix decreases gradually under conventional recovery methods, and the permeability of fracture increases slightly first and then decreases gradually. The shale matrix and fracture permeability both increase first and then decrease gradually under CO₂ enhanced recovery methods. Compared to conventional recovery methods, the injection of CO₂ for recovery leads to a faster decrease in CH₄ concentration within the shale matrix and fractures, with a higher CH₄ production. Nevertheless, the rate of CH₄ production increase exhibits a gradual deceleration as time progresses.
- 2) As the reservoir stress increases, the CH₄ production and CO₂ storage of the reservoir both decrease. The impact of high stress on the reduction of CH₄ production and CO₂ storage is mainly observed during the middle injection period, and it is primarily due to the coupling impacts of competitive adsorption and mechanical weakening. As the CO₂ injection pressure increases, CH₄ production and CO₂ storage capacity significantly increase. The promoting effect of high injection pressure on CH₄ pro-

- duction and CO_2 storage is mainly observed during the initial and middle periods, primarily due to the coupling impacts of chemical dissolution and pressure-driven mechanical weakening. As the injection temperature rises, CH_4 production and CO_2 storage capacity decrease, and the impact of injection temperature is mainly during the initial and middle periods.
- 3) The coupling effect of chemical dissolution-mechanical weakening caused by CO₂ injection in shale reservoirs is a crucial factor influencing shale gas recovery and CO₂ storage. The CH₄ production calculated by the model without incorporating the chemical dissolution-mechanical weakening coupling effect and that with only incorporating the chemical dissolution effect is significantly lower and higher, respectively, than the calculated value incorporating the coupling effect. Since CO₂-ESGR is a long-term process, it is essential to comprehensively incorporate the coupling impacts of chemical dissolution and mechanical weakening, competition adsorption-induced swelling, temperature effects, and effective stress.

Acknowledgements

This study was financially supported by the National Natural Science Foundation of China (No. 52404145), the National Science and Technology Major Project of China (No. 2024ZD1004304), the China Postdoctoral Science Foundation (Nos. 2024M753494 and 2024000132), Chongqing's Special Funding for Postdoctoral Research Projects (No. 2024CQB-SHTB3059), the Chongqing Natural Science Foundation General Project (No. CSTB2025NSCQ-GPX0557).

Supplementary file

https://doi.org/10.46690/ager.2025.11.07

Conflict of interest

The authors declare no competing interest.

Open Access This article is distributed under the terms and conditions of the Creative Commons Attribution (CC BY-NC-ND) license, which permits unrestricted use, distribution, and reproduction in any medium, provided the original work is properly cited.

References

- Bekeshov, D., Ashimov, S., Wang, Y., et al. Understanding gas-enhanced methane recovery in graphene nanoslits via molecular simulations. Capillarity, 2023, 6(1): 1-12.
- Cai, J., Jiao, X., Wang, H., et al. Multiphase fluid-rock interactions and flow behaviors in shale nanopores: A comprehensive review. Earth-Science Reviews, 2024, 257: 104884.
- Chen, Z., Li, R., Du, Y., et al. Effect of confinement on the vapor-liquid-liquid three-phase equilibrium during CO₂ utilization and sequestration in shale reservoirs. Advances in Geo-Energy Research, 2025, 16(3): 199-210.
- Choi, C., Kim, J., Song, J. et al. Analysis of shale property changes after geochemical interaction under CO₂ sequestration conditions. Energy, 2021, 214: 118933.
- Deng, H., Voltolini, M., Molins, S. Alteration and erosion of rock matrix bordering a carbonate-rich shale fracture. Environmental Science & Technology, 2017, 51(15): 8861-8868.
- Du, X., Gu, M., Liu, Z., et al. Enhanced shale gas recovery by the injections of CO₂, N₂, and CO₂/N₂ mixture gases. Energy & Fuels, 2019, 33(6): 5091-5101.
- Fang, C., Huang, Z., Wang, Q., et al. Cause and significance of the ultr-low water saturation in gas-enriched shale reservoir. Journal of Natural Gas Geoscience, 2014, 25(3): 471-476.
- Fatah, A., Mahmud, H., Bennour, Z., et al. Geochemical modelling of CO₂ interactions with shale: Kinetics of mineral dissolution and precipitation on geological time scales. Chemical Geology, 2022a, 592: 120742.
- Fatah, A., Mahmud, H., Bennour, Z., et al. The impact of supercritical CO₂ on the pore structure and storage capacity of shales. Journal of Natural Gas Science and Engineering, 2022b, 98: 104394.
- Kachanov, L. Rupture time under creep conditions. International Journal of Fracture, 1999, 97(1): 11-18.
- Khosravi, M., Kheirollahi, M., Liu, B., et al. Physicochemo-mechanical impact of sc-CO₂ on shale formations: The Bakken. Gas Science and Engineering, 2023, 112: 204945.
- Kim, T., Cho, J., Lee, K. Evaluation of CO₂ injection in shale gas reservoirs with multi-component transport and geomechanical effects. Applied Energy, 2017, 190: 1195-1206.
- Klewiah, I., Berawala, D., Walker, H., et al. Review of experimental sorption studies of CO₂ and CH₄ in shales. Journal of Natural Gas Science and Engineering, 2020, 73: 103045.
- Kuang, N., Zhou, J., Tian, S., et al. Fluid-solid coupling model with the multiple flow mechanism for CO₂-enhanced shale gas recovery and CO₂ sequestration. Energy & Fuels, 2024, 38(8): 7068-7084.
- Li, G., Li, G., Luo, C., et al. Dynamic evolution of shale permeability under coupled temperature and effective stress conditions. Energy, 2023a, 266: 126320.
- Li, N., Jin, Z., Wang, H., et al. Investigation into shale softening induced by water/CO₂-rock interaction. International

- Journal of Rock Mechanics and Mining Sciences, 2023b, 161: 105299.
- Li, Z., Elsworth, D. Controls of CO₂-N₂ gas flood ratios on enhanced shale gas recovery and ultimate CO₂ sequestration. Journal of Petroleum Science and Engineering, 2019, 179: 1037-1045.
- Liu, J., Xie, L., He, B., et al. Influence of anisotropic and heterogeneous permeability coupled with *in-situ* stress on CO₂ sequestration with simultaneous enhanced gas recovery in shale: Quantitative modeling and case study. International Journal of Greenhouse Gas Control, 2021, 104: 103208.
- Liu, S., Zhang, Y., Xing, W. Laboratory experiment of CO₂-CH₄ displacement and dispersion in sandpacks in enhanced gas recovery. Journal of Natural Gas Science and Engineering, 2015, 26: 1585-1594.
- Memon, S., Feng, R., Ali, M., et al. Supercritical CO₂-Shale interaction induced natural fracture closure: Implications for scCO₂ hydraulic fracturing in shales. Fuel, 2022, 313: 122682.
- Meng, S., Liu, C., Liu, Y., et al. CO₂ utilization and sequestration in organic-rich shale from the nanoscale perspective. Applied Energy, 2024, 361: 122907.
- Mansi M, Almobarak M, Ekundayo J, et al. Application of supervised machine learning to predict the enhanced gas recovery by CO₂ injection in shale gas reservoirs. Petroleum, 2024, 10(1): 124-134.
- Mohagheghian, E., Hassanzadeh, H., Chen, Z. CO₂ sequestration coupled with enhanced gas recovery in shale gas reservoirs. Journal of CO₂ Utilization, 2019, 34: 646-655.
- Ozotta, O., Kolawole, O., Malki, M., et al. Nano-to macroscale structural, mineralogical, and mechanical alterations in a shale reservoir induced by exposure to supercritical CO₂. Applied Energy, 2022, 326: 120051.
- Qin, C., Jiang, Y., Luo, Y., et al. Effect of supercritical CO₂ saturation pressures and temperatures on the methane adsorption behaviours of Longmaxi shale. Energy, 2022a, 206: 118150.
- Qin, C., Jiang, Y., Zhou, J., et al. Influence of supercritical CO₂ exposure on water wettability of shale: Implications for CO₂ sequestration and shale gas recovery. Energy, 2022b, 242: 122551.
- Song, Y., Song, Z., Chen, Z., et al. Simulation of CO₂ enhanced oil recovery and storage in shale oil reservoirs: Unveiling the impacts of nano-confinement and oil composition. Advances in Geo-Energy Research, 2024, 13(2): 106-118.
- Sun, Y., Wang, X., Meng, Y., et al. Fracture propagation mechanism and application of supercritical CO₂ fracturing in shale: A review. Petroleum Science, 2025, 22(4): 1625-1652.
- Tan, J., Xie, B., Lyu, Q., et al. Mechanical properties of shale after CO₂ and CO₂-based fluids imbibition: Experimental and modeling study. Rock Mechanics and Rock Engineering, 2022, 55(3): 1197-1212.
- Tang, C., Zhou, W., Chen, Z., et al. Numerical simulation of CO₂ sequestration in shale gas reservoirs at reservoir scale coupled with enhanced gas recovery. Energy, 2023,

- 277: 127657.
- Tian, S., Zhou, J., Xian, X., et al. Impact of supercritical CO₂ exposure time on the porosity and permeability of dry and wet shale: The influence of chemo-mechanical coupling effects. Energy, 2023a, 270: 126905.
- Tian, S., Zhou, J., Xian, X., et al. The impact of supercritical CO₂ exposure time on the effective stress law for permeability in shale. Energy, 2023b, 284: 129334.
- Wan, Y., Jia, C., Lv, W., et al. Recovery mechanisms and formation influencing factors of miscible CO₂ huff-n-puff processes in shale oil reservoirs: A systematic review. Advances in Geo-Energy Research, 2024, 11(2): 88-102.
- Wang, F. Key controls in shale gas production. University of Texas: Austin, John and Catherine Jackson School of Geosciences. 2010.
- Wang, Y., Dai, Z., Wang, G., et al. A hybrid physics-informed data-driven neural network for CO₂ storage in depleted shale reservoirs. Petroleum Science, 2024a, 21(1): 286-301.
- Wang, H., Huang, J., Zhan, S., et al. Study on CO₂ and CH₄ competitive adsorption in shale organic and clay porous media from molecular- to pore-scale simulation. SPE Journal, 2024b, 29(6): 3265-3276.
- Wang, H., Zhou, J., Xian, X., et al. Shale Gas Production and CO₂ Storage of CO₂-ESGR Based on the Stress-Strain-Sorption Behavior of Shale. Energy & Fuels, 2025, 39(11): 5406-5418.
- Wu, Y., Liu, J., Elsworth, D., et al. Evolution of coal permeability: Contribution of heterogeneous swelling processes. International Journal of Coal Geology, 2011, 88(2-3): 152-162.
- Yang, K., Zhou, J., Xian, X., et al. Effect of supercritical CO₂-water-shale interaction on mechanical properties of shale and its implication for carbon sequestration. Gas Science and Engineering, 2023, 111: 204930.
- Yang, K., Zhou, J., Xian, X., et al. Changes of wettability of shale exposed to supercritical CO₂-water and its alteration mechanism: Implication for CO₂ geo-sequestration. Fuel, 2024, 357: 129942.
- Yang, K., Zhou, J., Xian, X., et al. Chemical-mechanical coupling effects on the permeability of shale subjected to supercritical CO₂-water exposure. Energy, 2022, 248: 123591.
- Yi, J., Qi, Z., Li, X., et al. Spatial correlation-based machine learning framework for evaluating shale gas production potential: A case study in southern Sichuan Basin, China. Applied Energy, 2024, 357: 122483.
- Yin, H., Zhou, J., Jiang, Y., et al. Physical and structural changes in shale associated with supercritical CO₂ exposure. Fuel, 2016, 184: 289-303.
- Yuan, J., Jiang, R., Cui, Y., et al. The numerical simulation of

- thermal recovery considering rock deformation in shale gas reservoir. International Journal of Heat and Mass Transfer, 2019, 138: 719-728.
- Zeng, X., Li, B., Li, J., et al. New Model for gas transport in microfracture in shale reservoirs: Integration of effective stress, gas adsorption, and second-order slippage. Energy & Fuels, 2023, 37(18): 13880-13897.
- Zhang, N., Luo, Z., Chen, Z., et al. Thermal-hydraulic-mechanical-chemical coupled processes and their numerical simulation: A comprehensive review. Acta Geotechnica, 2023, 18(12): 6253-6274.
- Zhang, W., Mehrabian, A. Full coupling of CO₂-CH₄ transport and sorption with solid deformation in gas shale enhances natural gas recovery and geological CO₂ storage capacity. Journal of Natural Gas Science and Engineering, 2022, 106: 104736.
- Zhao, J., Wu, T., Pu, W., et al. Application status and research progress of CO₂ fracturing fluid in petroleum engineering: A brief review. Petroleum, 2024, 10(1): 1-10.
- Zhao, P., Xie, L., He, B., et al. Strategy optimization on industrial CO₂ sequestration in the depleted Wufeng-Longmaxi formation shale in the northeastern Sichuan basin, SW China: From the perspective of environment and energy. ACS Sustainable Chemistry & Engineering, 2020a, 8(30): 11435-11445.
- Zhao, X., Chen, Z., Wang, B., et al. A multi-medium and multi-mechanism model for CO₂ injection and storage in fractured shale gas reservoirs. Fuel, 2023, 345: 128167.
- Zhao, Y., Lu, G., Zhang, L., et al. Numerical simulation of shale gas reservoirs considering discrete fracture network using a coupled multiple transport mechanism and geomechanics model. Journal of Petroleum Science and Engineering, 2020b, 195: 107588.
- Zhou, J., Liu, G., Jiang, Y., et al. Supercritical carbon dioxide fracturing in shale and the coupled effects on the permeability of fractured shale: An experimental study. Journal of Natural Gas Science and Engineering, 2016, 36: 369-377.
- Zhou, J., Tian, S., Xian, X., et al. Comprehensive review of property alterations induced by CO₂-shale interaction: Implications for CO₂ sequestration in shale. Energy & Fuels, 2022, 36(15): 8066-8080.
- Zhou, J., Yang, K., Zhou, L., et al. Microstructure and mechanical properties alterations in shale treated via CO₂/CO₂-water exposure. Journal of Petroleum Science and Engineering, 2021, 196: 108088.
- Zou, Y., Li, S., Ma, X. Effects of CO₂-brine-rock interaction on porosity/permeability and mechanical properties during supercritical-CO₂ fracturing in shale reservoirs. Journal of Natural Gas Science and Engineering, 2018, 49: 157-168.